Acta Pharmaceutica Sinica B 2024;14(2):765−780

Chinese Pharmaceutical Association
Institute of Materia Medica, Chinese Academy of Medical Sciences

Acta Pharmaceutica Sinica B

www.elsevier.com/locate/apsb
www.sciencedirect.com

ORIGINAL ARTICLE

Dual-responsive supramolecular photodynamic nanomedicine with activatable immunomodulation for enhanced antitumor therapy

Siqin He[a,b], Lulu Wang[a], Dongxu Wu[b], Fan Tong[b], Huan Zhao[c], Hanmei Li[d], Tao Gong[b], Huile Gao[b,*], Yang Zhou[a,b,*]

[a]*Key Laboratory of Tropical Biological Resources of Ministry of Education, School of Pharmaceutical Sciences, Hainan University, Haikou 570200, China*
[b]*Key Laboratory of Drug-Targeting and Drug Delivery System, West China School of Pharmacy, Sichuan University, Chengdu 610041, China*
[c]*Revvity Inc., Waltham, MA 02451, USA*
[d]*School of Food and Biological Engineering, Chengdu University, Chengdu 610106, China*

Received 19 August 2023; received in revised form 13 October 2023; accepted 15 October 2023

KEY WORDS

Photodynamic therapy;
Immunosuppressive microenvironment;
Immunomodulator;
Dual-responsive;
Supramolecular assembly;
Checkpoint blockade

Abstract A major challenge facing photodynamic therapy (PDT) is that the activity of the immune-induced infiltrating $CD8^+$ T cells is subject to the regulatory T lymphocytes (Tregs), leaving the tumor at risk of recurrence and metastasis after the initial ablation. To augment the antitumor response and reprogram the immunosuppressive tumor microenvironment (TME), a supramolecular photodynamic nanoparticle (DACss) is constructed by the host-guest interaction between demethylcantharidin-conjugated β-cyclodextrin (DMC-CD) and amantadine-terminated disulfide-conjugated FFVLGGGC peptide with chlorin e6 decoration (Ad-ss-pep-Ce6) to achieve intelligent delivery of photosensitizer and immunomodulator for breast cancer treatment. The acid-labile β-carboxamide bond of DMC-CD is hydrolyzed in response to the acidic TME, resulting in the localized release of DMC and subsequent inhibition of Tregs. The guest molecule Ad-ss-pep-Ce6 can be cleaved by a high level of intracellular GSH, reducing photosensitizer toxicity and increasing photosensitizer retention in the tumor. With a significant increase in the CTL/Treg ratio, the combination of Ce6-based PDT and DMC-mediated immunomodulation adequately achieved spatiotemporal regulation and remodeling of the TME, as well as improved primary tumor and *in situ* lung metastasis suppression with the aid of PD-1 antibody.

*Corresponding authors.
E-mail addresses: gaohuile@scu.edu.cn (Huile Gao), yangzhou@hainanu.edu.cn (Yang Zhou).

Peer review under the responsibility of Chinese Pharmaceutical Association and Institute of Materia Medica, Chinese Academy of Medical Sciences.

https://doi.org/10.1016/j.apsb.2023.10.006

1. Introduction

Photodynamic therapy (PDT) is emerging as a minimally invasive, rapid, and secure treatment modality for superficial tumors such as breast cancer, which primarily resorts to the triad of photosensitizer, light, and oxygen, to produce reactive oxygen species (ROS) and induce tumor apoptosis[1−4]. More importantly, PDT can induce immunogenetic cell death (ICD) to augment the immune system's anti-tumor response for further cancer immunotherapy[5]. During this process, the release of tumor-associated antigen (TAA) from damaged tumor cells promotes the maturation of dendritic cells (DCs) and the infiltration of cytotoxic T lymphocytes (CTLs) into the tumor microenvironment (TME), which exert the most dominant killing effect on tumor cells and determine the efficacy of immune activation-related cancer therapy[6−8]. Despite the above strong superiority, in most cases, severe immunosuppression in the TME shapes the pattern and level of T-cell infiltration (T-cell homing) and activation, making it difficult to rely on ICD for complete tumor ablation or even possible risk of recurrence and metastasis[9−12]. Given these mechanisms, the combination of PDT and TME immunomodulation is necessary to further advance immunotherapy[13−15].

In addition to redox status, acidity, and several biochemical pathways, the activity of CTLs is largely suppressed by certain cell types, the most important of which are regulatory T lymphocytes (Tregs), a highly immunosuppressive subset of $CD4^+$ T cells that negatively regulate the immune response and impair CTL activity, thereby maintaining immune homeostasis and promoting tumor progression[16−20]. Reducing the number of Tregs in the immunosuppressive TME facilitates an increase in the number and activity of CTLs and better levels of anti-tumor immunity[21,22]. Demethylcantharidin (DMC), a protein phosphatase 2A (PP2A) inhibitor, shows potential as a TME immunomodulator[23]. It enhances tumor debulking by increasing the infiltration of CTL and reducing Treg numbers, without causing noticeable acute or chronic toxicity[24]. This effect is achieved through the inhibition of PP2A and activation of the mammalian target of rapamycin complex 1 (mTORC1) signaling pathway, resulting in reduced expression of forkhead box P3 (FOXP3) and hindering Treg formation in the TME[22]. Based on the immunomodulatory effects of DMC, the combination with photosensitizer is expected to play an important role in improving the efficacy of immunotherapy and tumor suppression.

Despite the combination is promising, delivering two components to different parts of the tumor to achieve a synergy effect is a significant challenge, especially given the disparities in hydrophilicity and pharmacokinetics between photosensitizer and immunomodulator. Nanotechnology has recently shown promising potential in drug co-delivery, particularly with the emergence of drug self-assembly systems[25−30]. Supramolecular self-assembly systems, specifically β-cyclodextrin (CD)-based systems, have been widely used for the delivery of many types of drugs[31−34]. CD's inherent hydrophilic surfaces and hydrophobic cavity enable the separate loading of DMC and photosensitizer, forming nanoparticles through host−guest non-covalent interactions[35−39]. Nevertheless, two challenges remain: (1) DMC is rapidly metabolized and its precise delivery to the TME is difficult; (2) photosensitizer suffers from phototoxicity. To overcome these challenges, a stimulus-responsive strategy was employed. DMC was modified on the β-CD surface *via* stimulus-activatable chemical bonds to create a prodrug system, which maintains an "off" state until exposure to a specific trigger in the TME to release drugs on demand for precise manipulation of immunomodulation. Similarly, photosensitizer was connected to a guest molecule module (such as amantadine) *via* stimulus-responsive chemical bonds. In this way, the nanoparticles can be degraded and retained in the tumor cells in response to specific signals, reducing phototoxicity due to the accumulation of the photosensitizer at non-target sites. Based on the above assumptions, the CD-based dual-responsive supramolecular prodrug self-assembly system holds great potential for the specific and accurate co-delivery of photosensitizer and DMC.

Although the combination of PDT and the immunomodulator DMC promotes $CD8^+$ T-cell infiltration and activation, there is an adaptive upregulation of PD-L1 expression on the surface of tumor cells, which may lead to T-cell dysfunction. This may be due to several factors: (1) PDT-mediated hypoxia *via* the hypoxia-inducible factor 1α (HIF-1α) signaling pathway[40]; (2) PDT-induced increased production of IFN-γ by lymphocytes[41,42]; (3) ROS-generated exogenous oxidative stress[43]; (4) DMC-mediated activation of the Akt signaling pathway through inhibition of PP2A[23,44,45]. The presence of these mechanisms reduces the therapeutic efficacy of the combination, so we integrated immunotherapy based on immune checkpoint blockade (ICB) therapy, PDT, and DMC, using PDT to increase T-cell infiltration, DMC to decrease the number of Tregs to alleviate the immunosuppressive TME, and PD-1 antibody to reverse T-cell dysfunction, ultimately leading to enhanced therapeutic efficacy.

Here, we designed a CD-based supramolecular self-assembled nanomedicine with photosensitizer and immunomodulator to restore the activity of T cells and remodel immunosuppressive TME. As illustrated in Scheme 1, hydrophilic DMC was modified on the surface of the host molecule β-CD using an acid-sensitive β-carboxamide bond. Simultaneously, the hydrophobic photosensitizer chlorin e6 (Ce6) was linked with amantadine group (Ad)-terminated peptide FFVLGGGC *via* disulfide bonds to form the hydrophobic core Ad-ss-pep-Ce6. Through host-guest recognition, DMC-CD and Ad-ss-pep-Ce6 self-assembled to form the DMC-CD/Ad-ss-pep-Ce6 nanoparticles (DACss). The immunomodulatory capacity of DMC on the surface of the nanoparticles in the physiological environment was in the "off" state. After passive accumulation in the tumor, the β-carboxamide bond in DMC-CD was hydrolyzed in the acidic TME and released DMC to suppress Treg formation. After entering into the tumor cells, the remaining

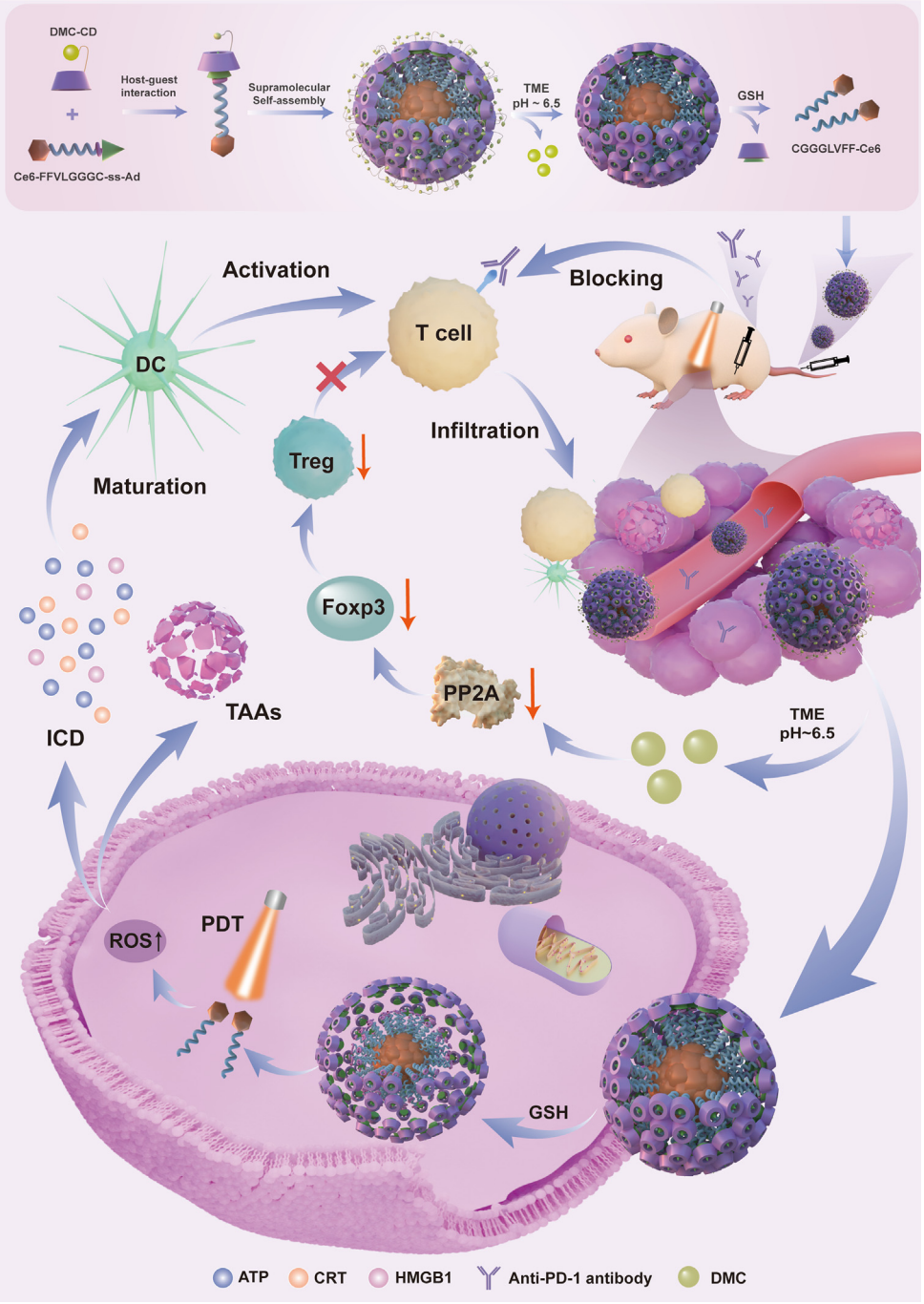

Scheme 1 Schematic illustration of the preparation and biological function of DMC-CD/Ad-ss-pep-Ce6 nanoparticles (DACss).

nanoparticles disintegrated in response to the high level of intracellular GSH, generating ROS under near-infrared light to ablate the tumor and induce ICD. With the improvement of the CTL/Treg ratio, the combination of Ce6-based PDT and DMC-mediated immunomodulation fully realized the spatiotemporal regulation of TME, which greatly enhanced the effect of photo-immunotherapy. Meanwhile, the combination with PD-1 antibody could counteract the PD-L1 upregulation on the membrane of tumor cells caused by PDT and DMC, improve the tumor suppression rate, and inhibit the occurrence of *in situ* lung metastasis.

2. Materials and methods

2.1. Materials

Ce6 was purchased from Frontier Scientific, Inc. (Logan, Utah, USA). β-CD and Mono-(6-amino-6-deoxy)-beta-cyclodextrin (short for β-CD-NH_2) were purchased from Zhiyuan Biotechnology Co., Ltd. (Binzhou, China). Peptides (NH_2-FFVLGGGC) were obtained from Sangon Biotech Co., Ltd. (Shanghai, China). DMC, DCFH-DA, and 3-(2-pyridyl dithiopropionic acid) were purchased

from Bidepharm (Shanghai, China). Anti-PD-1 antibody was purchased from BioXCell (West Lebanon, NH, USA). 1-(3-Dimethylaminopropyl)-3 ethylcarbodiimide hydrochloride (EDC), 4-dimethylaminopyridine (DMAP), *N*-hydroxysuccinimide (NHS), and trimethylamine (TEA) were purchased from Aladdin (Shanghai, China). Ad-Mal was purchased from Xi'an Qiyue Biotechnology Co., Ltd. (Xi'an, China). Alexa Fluro 647 Goat Anti-Rabbit IgG (H + L) secondary antibody, Goat Anti-Rabbit IgG H&L (FITC) antibody (ab6717), anti-calreticulin (CRT) antibody (ab92516), anti-mouse PD-L1 antibody (ab213480), anti-mouse high-mobility group box-1 protein (HMGB-1) (ab18256), and anti-mouse CD31 (ab222783) antibody were purchased from Abcam (Hongkong, China). PE-anti-mouse Foxp3 antibody (320008) and APC-anti-mouse CD40 antibody (124612) were purchased from Biolegend (San Diego, CA, USA). The Annexin V-fluoresceine isothiocyanate (FITC) apoptosis assay kit was obtained from Yeason (Shanghai, China). HMGB-1 ELISA detection kit was purchased from Quanzhou Ruixin Biotechnology (Quanzhou, China), the adenosine triphosphate (ATP) assay kit was achieved from Beyotime Biotechnology (Shanghai, China), and the PP2A ELISA detection kit was purchased from Jiangsu Meimian Industrial Co., Ltd. (Jiangsu, China). The murine 4T1 breast cancer cell line was obtained from the Chinese Academy of Sciences Cells Bank (Shanghai, China). Female BALB/c mice (5−6 weeks, 18−20 g) were obtained from SPF Biotechnology Co., Ltd. (Beijing, China). All animal experiments were approved by the Animal Experimentation Ethics Committee of Sichuan University.

2.2. Methods

2.2.1. Synthesis of DMC-modified CD

The synthesis process of DMC-CD is shown in Supporting Information Fig. S1. β-CD-NH_2 (100 mg), DMC (74.14 mg), and DMAP (5.39 mg) were thoroughly mixed in 4 mL of *N*, *N*-dimethylformamide (DMF) and stirred at 65 °C for at least 24 h. The reaction mixture was then dialyzed (MWCO500) in deionized water (pH ∼8.5) at room temperature for 8 h. After dialysis, the solution was collected and lyophilized. The product was characterized and verified by proton nuclear magnetic resonance (^{1}H NMR) spectrum (Agilent, DD2 600, USA) and Liquid Chromatography with Mass Spectrometry (LC−MS, PerkinElmer, USA).

2.2.2. Synthesis of Ad-ss-pep-Ce6 and Ad-pep-Ce6

The purchased peptide NH_2-FFVLGGGC (60 mg, 1 eq.) and Ad-ss-Py (31.41 mg, 1.2 eq.) were mixed in 3 mL DMF and stirred in the dark for 12 h at 30 °C under a nitrogen atmosphere to obtain Ad-ss-pep. Then Ce6 (53.84 mg, 1 eq.), EDC (28.10 mg, 3 eq.), and NHS (31.15 mg, 3 eq.) were dissolved in 2 mL DMF and stirred for 2 h at room temperature to activate the carboxyl of Ce6. The latter solution and TEA (37.52 μL, 3 eq.) were added into the former one and allowed to react for 24 h in the dark at 30 °C under a nitrogen atmosphere. The final collected solution was dialyzed with DMSO(MWCO1000) for 12 h and with deionized water for 24 h at room temperature.

The preparation of Ad-pep-Ce6 is similar to the Ad-ss-pep-Ce6, with only the first step being slightly different. The peptide NH_2-FFVLGGGC (60 mg, 1 eq.), Ad-Mal (45.45 mg, 2 eq.), and TEA (the pH of the solution was adjusted to 7.5) were mixed in DMF and stirred at 30 °C under a nitrogen atmosphere for 24 h. The subsequent reaction with Ce6 was the same as described above. The final product and intermediate product of Ad-ss-pep-Ce6 and Ad-pep-Ce6 were verified by ^{1}H NMR spectrum (Agilent), LC−MS (PerkinElmer), and matrix-assisted laser desorption/ionization time-of-flight mass spectrometry (MALDI-TOF-MS, SHIMADZU, AXIMA-TOF, Japan) (the matrix was sinapic acid).

2.2.3. Construction of DACss

The nanoparticles were prepared according to the previous literature[46]. In brief, DMC-CD and Ad-ss-pep-Ce6, dissolved in DMF, were mixed at a molar ratio of 1:1 and sonicated in a water-bath ultrasonic apparatus (40 W, 30 min) to form an inclusion complex. Subsequently, the mixed solution was added drop-by-drop into 15 times the volume of deionized water (pH ∼ 8.5) during stirring at room temperature (1000 rpm, 15 min). Then the mixture was ultrasonicated using an ultrasonic cell crusher for 5 min (65 W, 5 s/5 s/cycle) to make the nanoparticles more homogeneous in size. DMF was then removed and the solution was concentrated by centrifugal filters (10 kDa, Millipore) to obtain DACss. The same procedure was used to prepare AC, ACss, and DAC, with β-CD used as a DMC-free control for the host molecule in the AC and ACss groups, and Ad-pep-Ce6 as a guest molecule control in the AC and DAC groups, lacking GSH responsiveness.

2.2.4. In vitro pH-responsive DMC release

A 10 mmol/L aqueous solution of sodium acetate was prepared and the pH was adjusted with acetic acid to obtain release media for different pH conditions, and the DACss solution was loaded into a dialysis bag (MWCO1000) and incubated at 37 °C. At different time intervals, the content of DMC was determined by LC−MS (PerkinElmer), and the cumulative release at different times was calculated to obtain the release profile of DMC.

2.2.5. Cellular uptake and retention

1×10^5 4T1 cells were seeded into 12-well plates and incubated until they reached 80% confluency. The cells were then treated with different preparation groups (Ce6 concentration of 2 μg/mL) for 2 h, and the fluorescence signal of each group was measured using flow cytometry (Agilent NovoCyte, USA). For the qualitative assay, 4T1 cells were plated on coverslips in 12-well plates and treated as described above. Cells were then stained for lysosomes with Lysotracker Red DND-99, fixed with 4% paraformaldehyde, and then nuclei stained with DAPI for confocal imaging. The fluorescence intensity was observed using confocal microscopy (CLSM, Leica, Wetzlar Germany).

To prepare multicellular spheroids (MCSs), 4T1 cells (5×10^3 cells per well) were added to 96-well plates coated with 2% (*w*/*v*) low-melting-point gel. After approximately five days of incubation, spherical MCSs were selected and treated with Ce6, AC, ACss, DAC, and DACss. After 12 h of incubation, the drug-containing medium was replaced with a fresh DMEM medium for another 12 h. Then, the MCSs were washed, fixed, and observed by CLSM.

2.2.6. In vitro cytotoxicity and apoptosis assay

When 4T1 cells were seeded into 96-well plates (3×10^3 cells per well) and grew to 50% confluency, the fresh medium (as a control) or medium containing different formulations (Ce6+L, AC, AC + L, ACss, ACss + L, DAC, DAC + L, DACss, and DACss + L) at various Ce6 concentrations (0.625−10 μg/mL) were introduced into the wells. Irradiation (100 mW/cm^2, 20 s per well) was performed 12 h post-incubation. At 12 h post-irradiation, cytotoxicity was assessed by MTT assay.

For the apoptosis assay, 4T1 cells (1×10^5 cells per well) were placed in 12-well culture plates and incubated for 36 h. The cells were then treated with different formulations as described in the cytotoxicity assay. Irradiation was conducted after 12 h (100 mW/cm^2, 1 min). After 2 h, the cells were collected, stained with Annexin V-FITC and PI, and then measured by flow cytometry.

2.2.7. *In vitro PP2A activity assay*

2×10^5 4T1 cells were seeded into 6-well plates and incubated until they reached 80% confluency. The cells were then treated with DMC, AC, and DACss (DMC concentration of 3 μg/mL) for 6 h. Then cells were washed twice with PBS and lysed with RIPA lysis buffer for 15 min on ice. The lysates were centrifuged at 12,000 rpm for 15 min and the supernatants containing total cellular protein were collected. Protein quantification was performed using the BCA protein assay kit. The lysate was also used to detect PP2A phosphatase activity using the PP2A ELISA detection kit.

2.2.8. *In vitro ICD assessment and DC maturation*

4T1 cells were seeded onto a coverslip in a 12-well plate and incubated with different formulations. After 12 h of incubation, the cells were irradiated (100 mW/cm^2, 1 min) and then incubated for an additional 2 h. The cells were then washed, collected, and stained with an anti-CRT antibody (1:100) at 4 °C for 30 min. This was followed by incubation with a FITC-conjugated secondary antibody (1:500) at 4 °C for 15−20 min. Finally, they were measured by flow cytometry. In addition, the supernatants were collected for ATP detection and ELISA assay of HMGB-1.

For the DC maturation assay, bone marrow-derived dendritic cells (BMDCs) were extracted from the femur and tibia of 8-week-old female BALB/c mice and cultured in a Petri dish for 6 days. Concurrently, 4T1 cells were treated with different formulations as described above. The supernatants of the 4T1 cells were then collected and added to the BMDCs in 12-well plates. After a 24-h incubation period, the cells were washed, collected, and stained with anti-CD11c-FITC, anti-CD40-APC, anti-CD80-PE/CY7, and anti-CD86-APC/CY7. The cells were then measured by flow cytometry.

2.2.9. *In vivo biodistribution*

4T1 cells suspended in PBS were subcutaneously injected into the left mammary fat pads of female BALB/c mice (3×10^5 cells/mouse). After 12 days, mice bearing tumors of approximately 150 mm^3 were randomly divided into 5 groups ($n = 3$). Then, free Ce6, AC, ACss, DAC, and DACss, each with an equivalent Ce6 concentration of 3.5 mg/kg, were intravenously injected into the 4T1 tumor-bearing BALB/c mice. *In vivo* fluorescent imaging was carried out at 2, 6, 12, and 24 h using a Lumina III Imaging System (PerkinElmer, USA). After the final imaging, all the tumors and organs were dehydrated, frozen, sectioned, and imaged by CLSM (Leica).

2.2.10. *Validation of upregulation of PD-L1 induced by PDT and DMC*

The construction of 4T1 breast cancer models in BALB/c mice was carried out as previously described, with each mouse receiving a subcutaneous injection of 3×10^5 cells. After 10 days, when the tumors had reached approximately 100 mm^3, the mice were randomly divided into three groups ($n = 3$). The groups were treated with PBS, Ce6+L (4 mg/kg), and DMC (1 mg/kg) *via* tail-vein injection (Fig. 1A). 2 h post-injection, the Ce6+L group was subjected to irradiation for 5 min (650 nm, 100 W/cm^2). This treatment regimen was repeated every two days for a total of three cycles. On the eighth day, the mice were euthanized, and single-cell suspensions were prepared from the tumors. These were then stained with anti-PD-L1-APC and analyzed *via* flow cytometry to assess the expression of PD-L1.

2.2.11. *Anti-tumor therapy*

4T1 cells were initially subcutaneously injected into the left mammary fat pads of female BALB/c mice (2×10^5 cells/mouse). After 9 days, when the tumor sizes reached approximately 60 mm^3, the tumor-bearing mice were randomly divided into eight groups ($n = 5$). These groups were intravenously injected with PBS, Ce6+L, DMC, AC + L, DAC + L, DACss, DACss + L, and DACss + L + anti-PD-1 (1 mg/kg DMC, 4 mg/kg Ce6), respectively. At the 4-h post-injection, the laser groups were irradiated for 5 min (650 nm, 100 W/cm^2). The treatments were repeated every 5 days for 3 cycles, while tumor volumes and body weights were recorded every 2 days. The PD-1 antibody was injected intraperitoneally in the DACss + L + anti-PD-1 group at a dose of 100 μg per mouse 24 h after laser irradiation, repeated 3 times starting from the second administration cycle. Tumor volume was calculated as 0.5 × length × width^2, measured *via* a caliper. After 31 days, the mice from all groups were euthanized and the major organs and tumors were collected and washed with PBS for subsequent histological analysis of hematoxylin and eosin (H&E), terminal deoxynucleotidyl transferase-mediated dUTP-biotin nick end labeling (TUNEL), and Ki67 staining assay. Additionally, the total number of *in situ* lung metastatic lesions was counted to evaluate the anti-metastatic effects of each group ($n = 5$).

2.2.12. *Immune response*

Fresh lymph nodes, spleens, and tumors from each group were collected to prepare single-cell suspensions. Anti-CD11c-FITC, anti-CD80-PE/CY7, and anti-CD86-APC were used for DC maturation in lymph nodes and spleen. To evaluate the level of T cells, splenocytes were stained with anti-CD3, anti-CD4, and anti-CD8; tumor cells were stained with anti-CD3, anti-CD4, anti-CD8, anti-PD-L1, and anti-Foxp3. For the investigation of memory T cell response, splenocytes were stained with anti-CD3, anti-CD44, and anti-CD62L. Cytokines in the tumor tissue homogenate, including TNF-α, TGF-β, IFN-γ, IL-1β, IL-2, IL-6, IL-10, and IL-12, were measured by ELISA kits according to the protocols.

3. Results and discussion

3.1. *Pre-validation of PD-L1 upregulation induced by PDT and DMC*

Phototherapy and DMC treatment have been reported to cause an adaptive upregulation of PD-L1 receptors on the surface of tumor cells, leading to the dysfunction of T cells. When comparing the three groups, we observed higher levels in both the DMC and Ce6+L groups, which were 1.8- and 2.5-fold higher than the control group, respectively (Fig. 1B and C). The results from the immunofluorescent images were consistent with those from the flow cytometry (Fig. 1D). This may reflect the immunosuppressive mechanism of residual cancer cells in

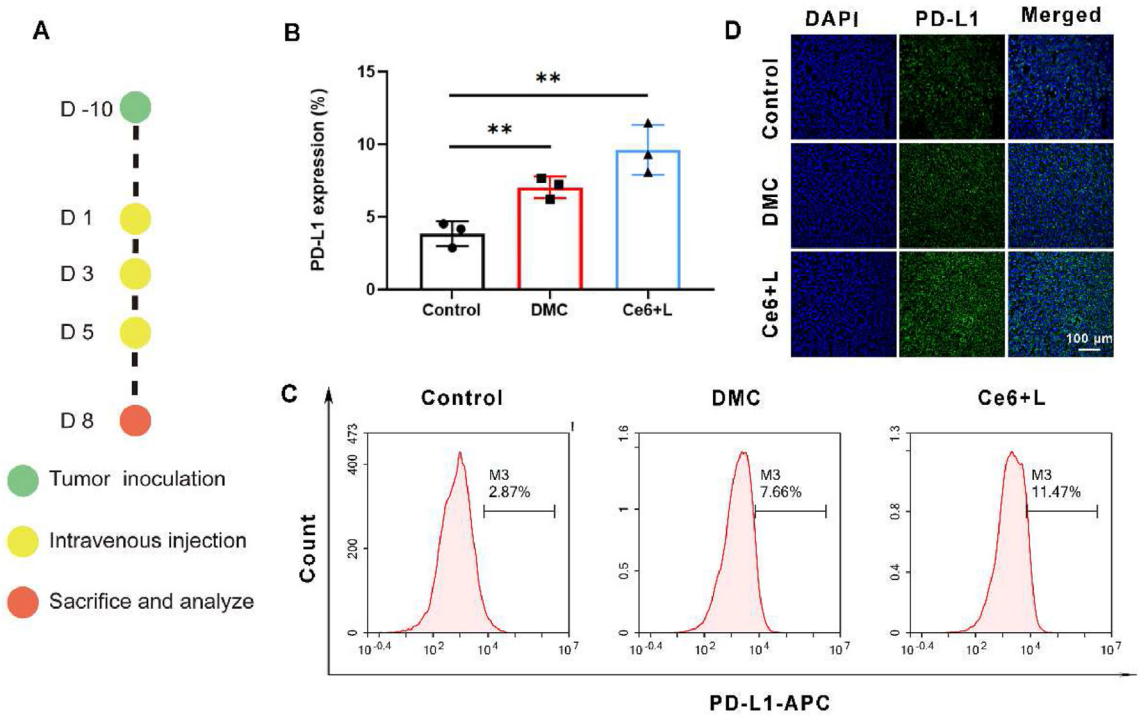

Figure 1 Validation of PD-L1 upregulation induced by PDT and DMC in 4T1 tumor-bearing mice. (A) Schematic illustration of the administration process. (B) Quantitative data and (C) representative flow cytometry plots of PD-L1 expression in tumors for each treatment group. Data are presented as mean ± SD ($n = 3$). $^{**}P < 0.01$. (D) Immunofluorescent images of PD-L1 expression in tumors. Scale bars represent 100 μm.

response to PDT and DMC, underscoring the need for further incorporation of PD-L1 blockade for further immunotherapy.

3.2. *Characterization of DACss*

Besides the peaks around δ_H 3.55 , δ_H 3.8, and δ_H 5.0 in β-CD-NH_2, the critical peaks of DMC around δ_H 1.64, δ_H 2.90, and δ_H 4.85 were also observed in DMC-CD (Supporting Information Fig. S2). The peaks at *m/z* around 1302.0 belonged to DMC-CD, further confirming the successful synthesis (Supporting Information Fig. S3). For the guest molecule, the peaks at *m/z* around 1616.22 and 1678.80 belonged to Ad-ss-pep-Ce6 and Ad-pep-Ce6 (Supporting Information Fig. S4), respectively, suggesting their successful synthesis. The MALDI-TOF-MS assay showed that the disulfide bond in Ad-ss-pep-Ce6 (1616.22) was cleaved to produce Ce6-pep-SH (1376.47) after incubation with 10 mmol/L GSH, confirming that the disulfide-bound Ad-ss-pep-Ce6 has good reduction sensitivity (Fig. S4). Based on the literature[46], we constructed DACss autonomously by supramolecular interactions using a 1:1 molar ratio of DMC-CD and Ad-ss-pep-Ce6 (Fig. 2A). The supramolecular inclusion complex was characterized by MALDI-TOF-MS (Supporting Information Fig. S5). When the host and guest molecules were physically mixed, the peaks of DMC-CD and Ad-ss-pep-Ce6 were observed at *m/z* around 1300 and 1600, respectively. After the formation of the inclusion complex, these two peaks weakened and the peak of the inclusion complex appeared at *m/z* around 2900, this result proved that the two formed the inclusion complex.

Subsequently, we performed a series of characterizations of DACss and its controls. The hydrodynamic sizes of AC, ACss, DAC, and DACss were 72.98 ± 3.20, 72.72 ± 3.81, 72.46 ± 2.48, and 73.67 ± 1.80 nm respectively, and appeared spherical under transmission electron microscopy (TEM) imaging (Fig. 2B–D and Supporting Information Table. S1). Moreover, all nanoparticles showed good uniformity, as confirmed by the polydispersity index, and had a negatively charged surface with a zeta potential from −20 to −30 mV (Fig. 2E and Supporting Information Table. S1). Furthermore, the four groups of nanoparticles showed excellent stability and biosafety. As seen in Fig. 2F and Supporting Information Fig. S6A and S6B, the nanoparticles could be maintained in water, high-salt solution, and 5% glucose solution with negligible size changes for 96 h. Fig. 2G and Fig. S6C showed the nanoparticles did not cause obvious hemolysis even at the concentration of up to 200 μg/mL (<10% hemolysis), indicating good biocompatibility and stability in the blood circulation of all nanoparticles. The release profile of DMC from DACss was determined and, as seen in Fig. 2H, the release rate of DMC was faster at pH 5.5 than at pH 7.4, indicating that the β-carboxamide successfully responded to the acidic pH and released DMC. Moreover, the nanoparticles had similar absorption peaks at 405 and 650 nm and emission peak at 650 nm (Fig. 2I and J), suggesting great potential for real-time *in vivo* tracking and photoregulation.

3.3. *Cellular uptake and retention, ROS generation, in vitro cytotoxicity studies, and PP2A activity assay*

The cellular uptake abilities of nanoparticles were evaluated using confocal imaging and flow cytometry. As shown in Fig. 3A, the uptake of DACss was time-dependent, with an increase in

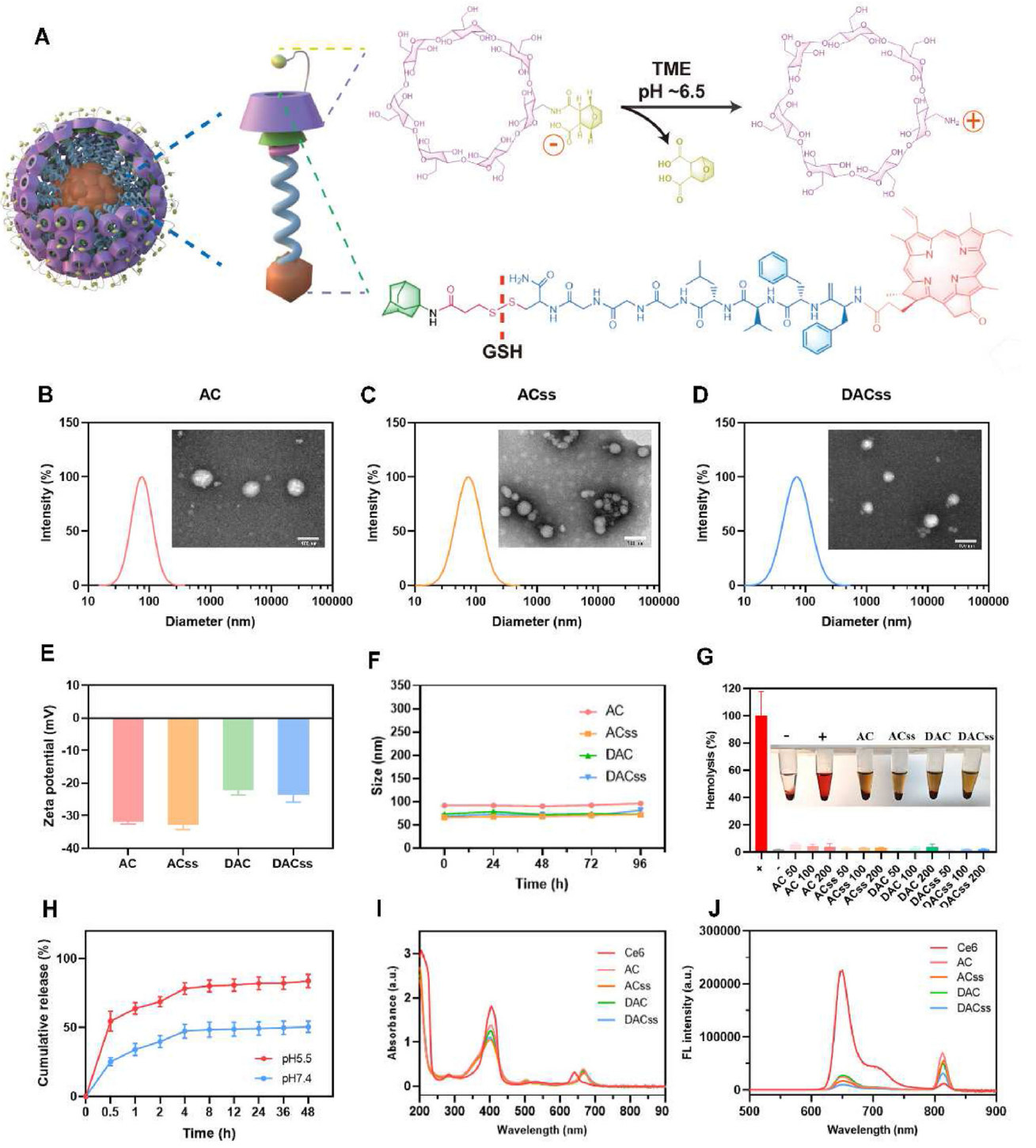

Figure 2 Characterization of nanomedicines and responsiveness. (A) Chemical structure of DACss and mechanism of pH-responsive DMC release and GSH response. Hydrodynamic diameters and TEM images of (B) AC, (C) ACss, (D) DACss. The scale bars represent 100 nm. (E) Zeta potential of AC, ACss, DAC, and DACss. (F) The stability of nanoparticles in water for 96 h. (G) Hemolysis analysis of red blood cells (RBCs) with different treatments for 2 h. Inset: images of RBCs after incubation with Triton X-100, PBS buffer, and groups of nanoparticles in PBS buffer at an equivalent dose (50 μg/mL for Ce6) followed by centrifugation. 1 × PBS buffer was used as a negative control (−), and Triton X-100 was used as a positive control (+). (H) Cumulative release of DMC at different pH from the DACss. (I) UV−Vis absorption and (J) fluorescence spectra of free Ce6 and the nanoparticles. Data are presented as mean ± SD ($n = 3$).

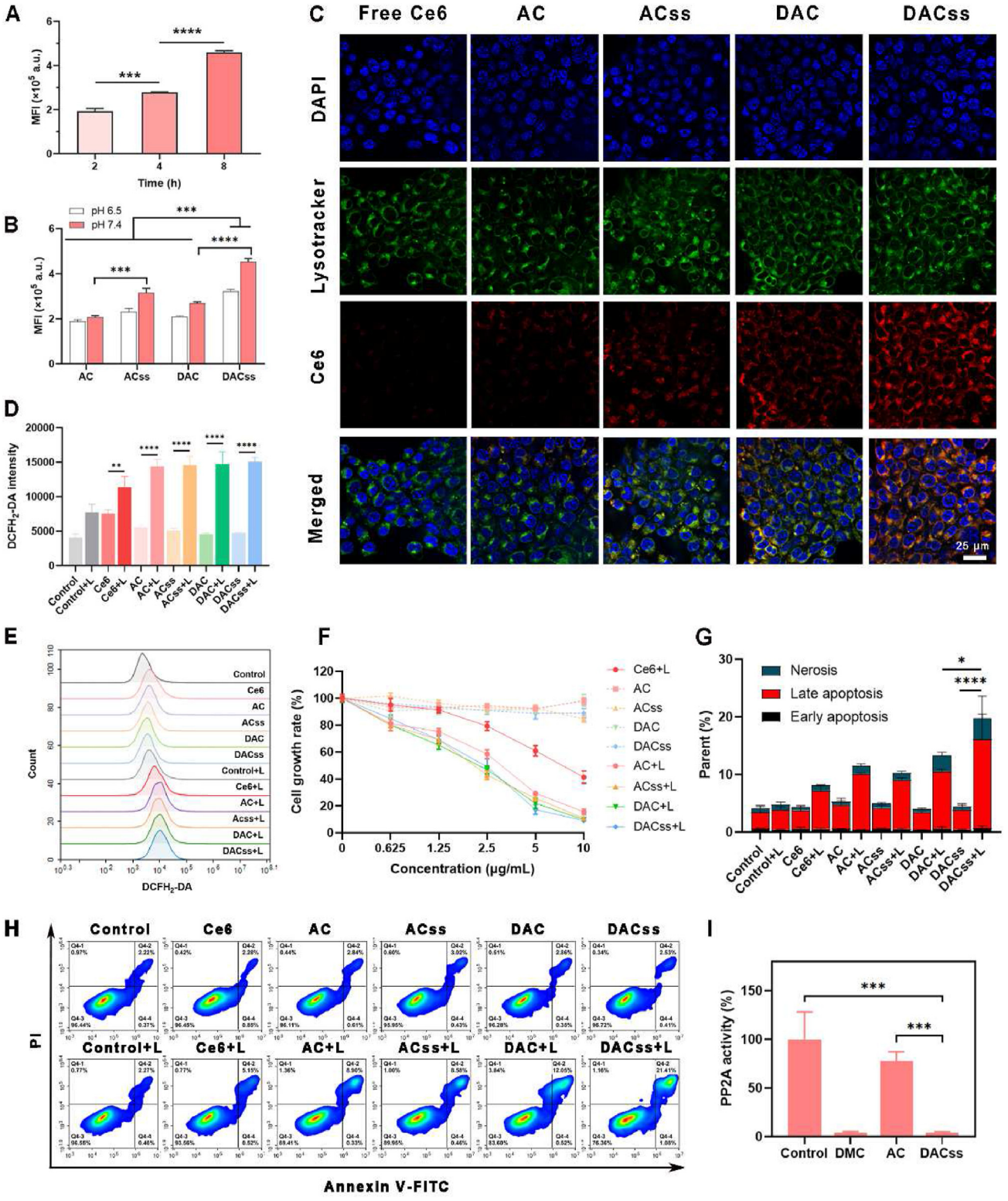

Figure 3 Cellular uptake, ROS generation, *in vitro* cytotoxicity studies, and PP2A activity assay. (A) The uptake of DACss at different time points is shown. (B) The uptake of four groups of nanoparticles at pH 6.5 and 7.4 conditions for 2 h. (C) CLSM images of cellular uptake for 2 h. Scale bars represent 25 μm. (D) Quantitative results and (E) representative flow cytometric images of intracellular ROS in 4T1 cells after incubation with different formulations in the presence or absence of laser irradiation by DCFH-DA probe. Data are presented as mean ± SD ($n = 3$). (F) Relative cell growth rate of 4T1 cells after being treated with free Ce6 and nanoparticles at different Ce6 concentrations with or without laser irradiation. Error bars indicate SD ($n = 4$). (G) Statistical graph and (H) representative flow cytometric images of apoptosis results. Error bars indicate SD ($n = 3$). (I) PP2A activity of 4T1 cells after incubation with DMC (3 μg/mL), AC, and DACss for 8 h. The PP2A activity of control cells was indicated as 1. Data are presented as mean ± SD ($n = 3$). $^{*}P < 0.05$, $^{**}P < 0.01$, $^{***}P < 0.001$, $^{****}P < 0.0001$.

fluorescent signals from intracellular nanoparticles as the uptake time increased. Importantly, the intensity of DACss at pH 7.4 and 6.5 for 2 h was 1.7- and 1.5-fold higher than DAC, consistent with the results of confocal imaging (Fig. 3B and C), implying that DACss can be more internalized by 4T1 cells when compared with other groups. We attributed this result to the disassembly of DACss in response to the high intracellular level of GSH. This led to the shedding of the hydrophilic CD shell and the formation of the CGGGLVFF-Ce6 structure, which was more hydrophobic and less likely to be cleared from the cell. As a result, exocytosis was reduced compared to the DAC group, leading to increased uptake at this time point, compared to the other groups. To prove the above conjecture, we introduced 4T1 MCSs for verification. Likewise, the DACss group showed the most robust retention effect compared to the free Ce6 and the other three nanoparticles in 4T1 MCSs (Supporting Information Fig. S7). This result confirmed the responsive retention of DACss.

The DCFH-DA probe was employed to detect the concentration of intracellular ROS generated by PDT. As depicted in Fig. 3D and E, with the addition of the laser, several groups of nanoparticles were able to produce a higher ROS level compared to the free Ce6 as well as the groups without the laser, indicating that the nanoparticles could enter into cells more and produce more ROS to eradicate tumor cells. The cytotoxicity of the DACss was verified by MTT experiments. As seen in Fig. 3F, the nanoparticle groups exhibited stronger cytotoxicity compared to free Ce6 after laser irradiation, while they were essentially non-toxic in the absence of laser irradiation, suggesting that the nanoparticles had a good biosafety profile. The MTT results also showed that low concentrations of free DMC had no significant killing effect (Supporting Information Fig. S8B). In addition, we examined the toxicity of these agents on HUVEC cells (Fig. S8C), and it can be seen that the toxicity of the DACss + L on HUVEC was lower than that on 4T1 cells, indicating that normal cells were well tolerated to the DACss + L. Furthermore, the DACss + L group resulted in the strongest killing effects, including 18% late apoptosis and 4% early apoptosis, which was higher than the ACss + L and DAC + L groups, as shown by the results of the FITC and PI double-staining assay assays (Fig. 3G and H). These results jointly suggested that DACss exhibited excellent anti-tumor activity at the cellular level.

To verify the immunomodulatory effect of DMC, we examined the effect of DACss on PP2A activity in 4T1 cells. As shown in Fig. 3I, the PP2A activity was significantly reduced in the DMC and DACss groups, both below 10%, whereas PP2A activity remained unchanged after treatment with AC, indicating the PP2A inhibitory ability of DACss.

3.4. *ICD and BMDC maturation*

We first evaluated the signals underlying the indicators of ICD. The mean fluorescence signals of CRT in the laser-irradiated group were significantly enhanced compared with those without laser irradiation (Fig. 4A and B, and Supporting Information Fig. S9). In this context, the mean fluorescence intensity of the DACss + L group was 2.9-fold higher than that of the DACss group. Likewise, all groups treated with PDT released a noticeable amount of ATP compared to the control and groups without laser irradiation (Fig. 4C). Among them, the released ATP concentration of the DACss + L group was the highest, which was 25.5- and 1.8-fold higher than the control and DAC + L groups, respectively. Similar results were obtained for the detection of extracellular HMGB-1 concentration (Fig. 4D), but the confocal results differed from this, as can be seen from Supporting Information Fig. S10, HMGB-1 was mainly distributed in the nucleus, with the highest fluorescence signals in the control group, and the signals were all very low in the nanoparticle laser groups, suggesting that the nanoparticle laser groups secreted HMGB-1 into extracellular roles, and thus the corresponding content in the nucleus was low. Subsequently, we used BMDCs to confirm the maturation of DCs. As shown in Fig. 4E and F, compared with the control and groups without laser irradiation, the percentage of $CD40^{+}CD86^{+}$ BMDCs in DACss+L significantly increased, which was 2.1- and 1.1-fold more than those of the control and DAC + L groups, respectively. These results indicated that PDT can potentially produce effective ICD, leading to the exposure of adequate TAAs to mature DCs and activate a potent anti-tumor immune response.

3.5. *In vivo biodistribution*

The *in vivo* targeting of the nanoparticles was investigated in a 4T1 tumor-bearing nude BALB/c model. As shown in Figs. 5A and 2 h post-injection, the free Ce6 group was distributed across the body, followed by rapid elimination from the liver and kidneys, while the other four nanoparticle groups showed stronger tumor site distribution and longer elimination time. According to the *ex vivo* results (Fig. 5B), the DACss showed the strongest retention effect. The semi-quantitative results also showed that its accumulation in the tumor was significantly 3.4-, 1.8-, and 1.3-fold more than the control, AC, and DAC groups (Fig. 5C). Similar results were obtained by confocal imaging of the tumor and major organ slices (Fig. 5D and Supporting Information Fig. S11). The distribution in the main organ exhibited in Fig. 5E, suggests that the liver and kidney were the main metabolism organs for Ce6.

3.6. *In vivo anti-tumor and lung metastasis performance*

The *in vivo* effects of DACss-mediated photo-immunotherapy and the suppression of *in situ* lung metastases were further evaluated in 4T1 tumor-bearing BALB/c mice (Fig. 6A). As depicted in Fig. 6B and Supporting Information Fig. S12A, the control group and the two single-agent groups, Ce6+L and DMC, exhibited the steepest growth trend, followed by the DACss group without laser treatment. All nanoparticle groups with laser irradiation demonstrated strong tumor-suppressing effects. The average tumor volume in the DACss + L + anti-PD-1 group maintained a slow growth rate and was below 300 mm^3 on Day 31, with a final tumor growth inhibition rate of 73.7% (considering control group as 0%), which was 1.1-, 1.3-, and 4.4-fold higher than that of the DACss + L (65.3%), DAC + L (57.6%), and DACss (16.8%) groups, respectively. In addition, the tumor weights and *ex vivo* tumor image results were highly compatible (Fig. 6C and D). To further validate this, the results of immunohistochemistry Ki67 and immunofluorescence TUNEL staining confirmed that the DACss + L + anti-PD-1 group had a superb anti-tumor effect (Fig. 6E and F). Fortunately, no significant change was observed in body weights in all groups during the treatment period (Fig. S12B), while H&E staining indicated no obvious histopathological damage in major tissues, indicating the good biocompatibility and biosafety of DACss (Supporting Information Fig. S13).

Considering the highly aggressive nature of 4T1 cancer cells, we also evaluated the potential anti-metastatic effect of DACss in

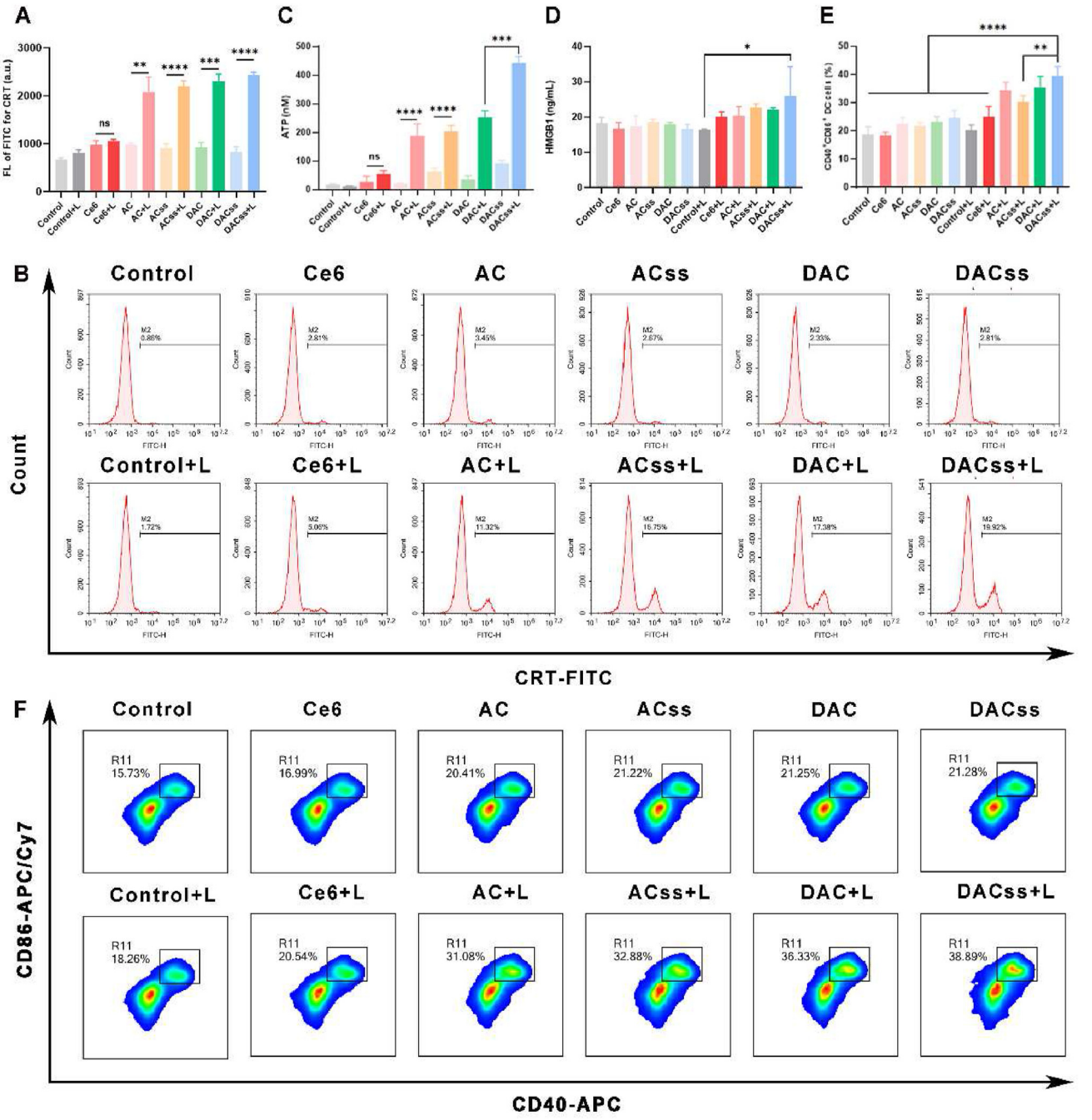

Figure 4 ICD-induced immune response and BMDC maturation. (A) Flow cytometry analysis and (B) representative flow cytometric images of CRT on the surface of 4T1 cells. (C) Extracellular ATP level and (D) HMGB-1 level in 4T1 cells treated with different nanoparticles. (E) Flow cytometry analysis of the percentages of $CD40^{+}CD86^{+}$ cells gated on $CD11c^{+}$ BMDCs incubated with culture supernatants of 4T1 tumor cells treated with different formulations. (F) Representative flow cytometric images of BMDC maturation. Data are presented as mean ± SD ($n = 3$). $^{*}P < 0.05$, $^{**}P < 0.01$, $^{***}P < 0.001$, $^{****}P < 0.0001$. ns, not significant.

the lungs. Consistent with previous tumor volume results, DACss + L + anti-PD-1 exerted the best anti-metastatic effect with the lowest number of the mean metastatic nodules, suggesting the therapeutic potential against metastatic tumors (Fig. 6G and Supporting Information Fig. S14). Meanwhile, H&E staining showed a consistent trend (Fig. 6H). Overall, DACss + L with the presence of PD-1 antibody could confer an effective inhibition of *in situ* lung metastases.

3.7. *The amelioration of immunosuppressive TME*

Before examining the immunological effects, we performed immunofluorescence staining of PD-L1 levels in all groups. As seen in Fig. 7A and B, the synergistic effect of DMC and Ce6 led to a significant increase in PD-L1 levels at the tumor site in both the DACss + L and DACss + L + anti-PD-1 groups, further validating the need for co-administration of PD-1 antibody.

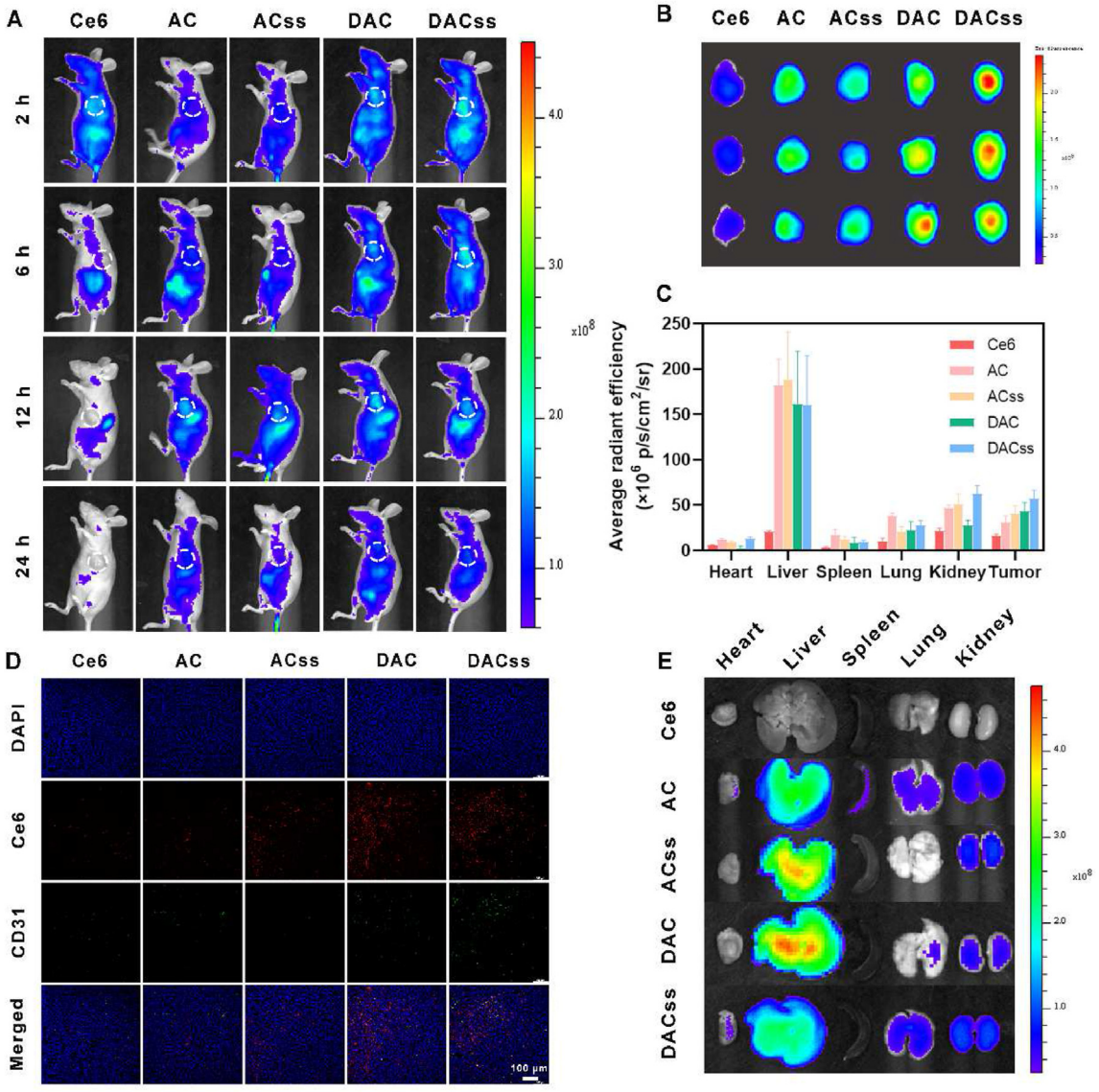

Figure 5 Evaluation of *in vivo* biodistribution. (A) Fluorescence images of 4T1 tumor-bearing nude BALB/c mice 2, 6, 12, and 24 h after intravenous injection. (B) *Ex vivo* fluorescent imaging of tumors 24 h post intravenous injection with different nanoparticles. (C) Semi-quantification of major organs and tumors 24 h post-injection. (D) Confocal images of frozen tumor slices. Nanoparticle groups carried their fluorescence signals for Ce6, nuclei were stained by DAPI, and vessels were stained green with an anti-CD31 antibody. (E) *Ex vivo* fluorescent imaging of main organs 24 h post intravenous injection. Data are presented as mean ± SD ($n = 3$). The scale bar represents 100 μm.

Subsequently, we examined the secretion of HMGB-1 and the expression of CRT in tumor tissues, both of which are critical for DC migration and maturation. Intensified red fluorescence signals of HMGB-1 and CRT were detected in the tumor sections of groups containing Ce6 (Fig. 7A and Supporting Information Fig. S15), indicating the generation of ICD by Ce6-mediated PDT, with the strongest signals in the DACss + L + anti-PD-1 group. We then examined the maturation of DCs in lymph nodes and spleen using flow cytometry. The DACss + L + anti-PD-1 group significantly promoted DC maturation in lymph nodes and spleens (Fig. 7C−E and Supporting Information Fig. S16), with the percentages of $CD80^+CD86^+$ cells 1.9- and 1.5-fold higher than control and AC + L groups, respectively. $CD80^+CD86^+$ DCs in the lymph nodes of control and drug-free groups remained at a lower level. Similar results were observed in the spleen. These results indicated that DACss induced substantial ICD, but was followed by adaptive upregulation of PD-L1 on the tumor surface.

The immunosuppressive TME tends to promote tumor escape and progression, severely undermining the anti-tumor process. To validate the ability of photosensitizer and immunomodulator to synergistically enhance anti-tumor immunity and convert the immunosuppressive "cold" TME into an immunogenic "hot" T cell-infiltrated TME, we measured the relevant infiltrating lymphocytes and cytokines at the tumor site. DACss-mediated photoimmunotherapy resulted in a significant increase in $CD3^+$ T cells. The DACss+L + anti-PD-1 group reached 20.7 ± 4.1% $CD3^+$ T cells, which was 2.6 times higher than the control group.

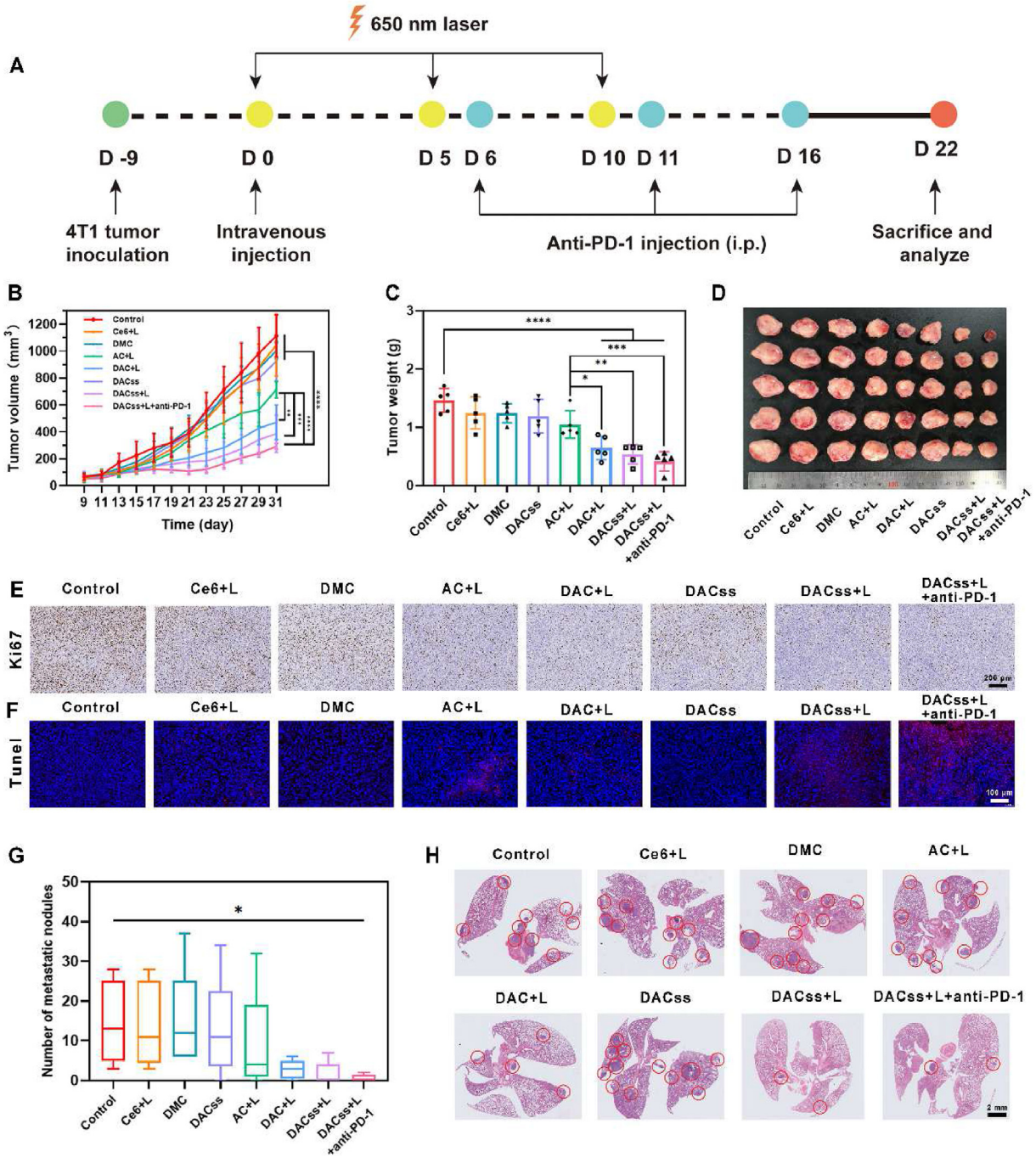

Figure 6 *In vivo* anti-tumor and anti-metastasis effects. (A) Schematic illustration of the combined therapy experiment design *in vivo*. (B) Tumor growth profiles after different treatments were recorded every two days for 22 days. (C) Corresponding tumor weights of mice on Day 22 following indicated treatments. Data are shown as mean ± SD ($n = 5$). (D) Photographic image of tumors at the end of the treatment. (E) Ki67 and (F) TUNEL staining images of tumor slices. The scale bar represents 200 and 100 μm, respectively. (G) Statistical results and (H) H&E images of the number of metastatic nodules in the lungs. Scale bar: 2 mm. Data are shown as mean ± SD ($n = 5$). $^{*}P < 0.05$, $^{**}P < 0.01$, $^{***}P < 0.001$, $^{****}P < 0.0001$.

Moreover, a larger proportion of infiltrated $CD4^+$ T cells and cytotoxic $CD8^+$ T cells was observed in the Ce6-mediated photodynamic immunotherapy group (Fig. 8A−C). $CD8^+$ T cells in tumors of DACss+L + anti-PD-1 reached 12.9%, which was enhanced by 1.2- and 6.8-fold when compared with DACss + L and control groups. Interestingly, as seen in the AC + L group (Fig. 8C−E and Supporting Information Fig. S17), Ce6-mediated PDT alone enhanced $CD8^+$ T cell infiltration, accompanied by increased tumor infiltration of Tregs. However, the effect of Tregs was attenuated by the DMC-containing groups, with the percentage of Tregs decreasing to 5.8 ± 1.7% and 4.9 ± 1.6% in the DAC + L and DACss + L groups, respectively, compared to the AC + L group (6.5 ± 0.9%). Specifically, the DACss + L + anti-PD-1 group restored Treg levels to the control

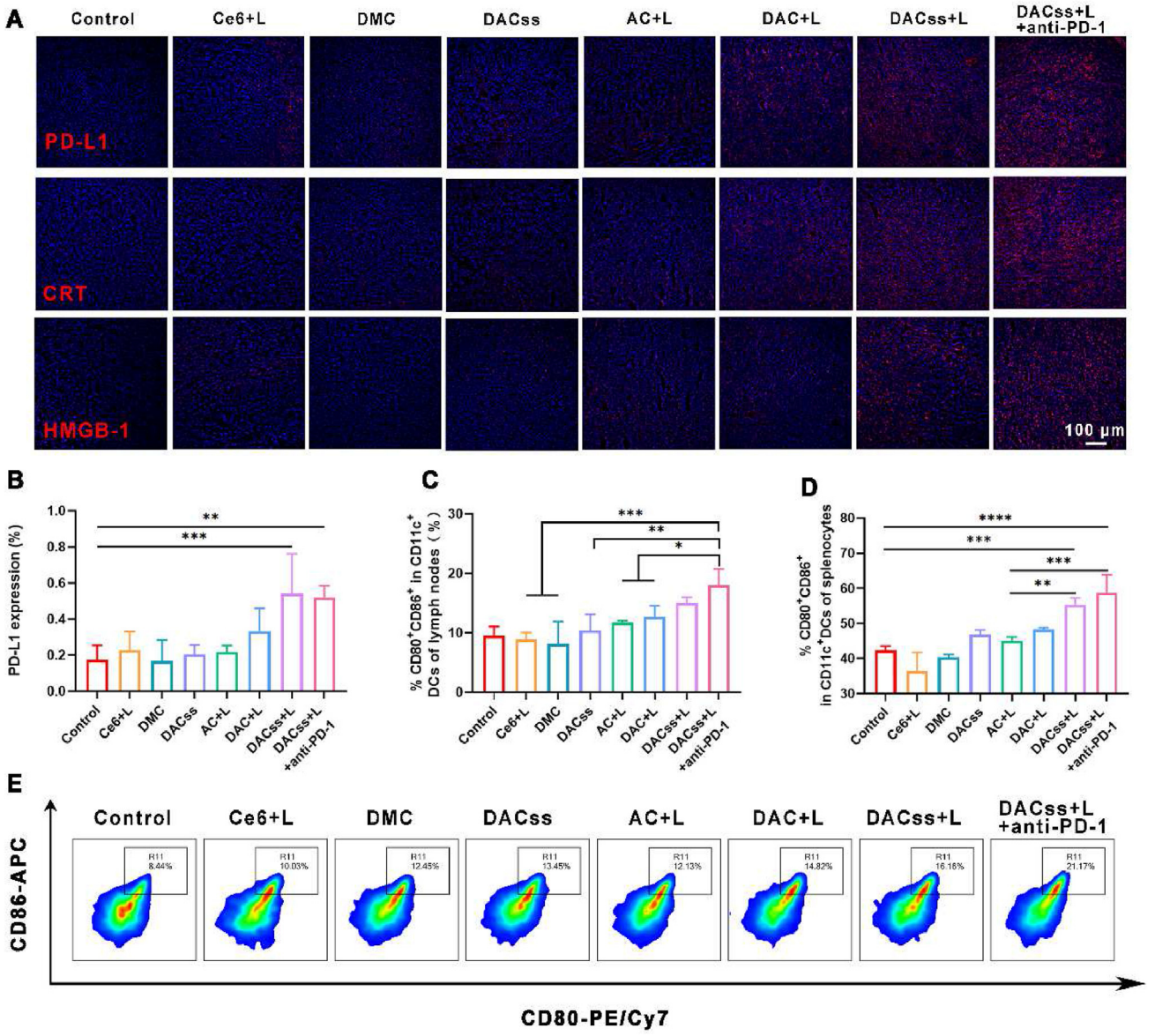

Figure 7 (A) Immunofluorescent images of PD-L1, CRT, and HMGB-1 in tumors. Scale bars represent 100 μm. (B) Quantification data of PD-L1 expression in tumors in each treatment group. Flow cytometry analysis of percentages of $CD80^+CD86^+$ cells gated on $CD11c^+$ cells in the (C) lymph nodes and (D) spleen of each treatment group. (E) Representative flow cytometry plots of $CD80^+CD86^+$ cells gated on $CD11c^+$ cells in the lymph nodes. Data are shown as mean ± SD ($n = 4$). $^*P < 0.05$, $^{**}P < 0.01$, $^{***}P < 0.001$, $^{****}P < 0.0001$.

group and showed the highest $CD8^+$ T/Treg cell ratio of all groups, possibly due to the combined effect of PDT, DMC, and ICB therapy. Moreover, DACss + L + anti-PD-1 treatment induced the highest population of IFN-γ-producing $CD8^+$ T cells, indicating the excellent activity of T cells infiltrating the TME (Fig. 8F). High secretion levels of pro-inflammatory cytokines in tumors including IFN-γ, TNF-α, IL-2, and IL-12 supported that the DACss + L + anti-PD-1 group realized effective tumor inhibition. In addition, IL-1β, IL-6, IL-10, and TGF-β, which are tumor immunosuppression indicators, were also reduced after treatment (Fig. 8G and Supporting Information Fig. S18).

Furthermore, we examined the infiltration of $CD4^+$ and $CD8^+$ T cells in the spleen (Supporting Information Fig. S19), which is consistent with the results in the tumors described above. To further confirm the immunological memory induced by DACss with 650 nm laser irradiation, the ratios of central memory T cells (Tcm, $CD44^+CD62L^+$) and effector memory T cells (Tem, $CD44^+CD62L^-$) in spleens were determined (Fig. 8H–J). In comparison to the control group (Tcm: 6.0 ± 0.2%, Tem: 11.1 ± 1.8%), DACss + L + anti-PD-1 exhibited a much higher level of memory T cells (Tcm: 15.3 ± 3.3%, Tem: 45.1 ± 3.9%), confirming the induction of local immunological memory and the potential of long-term immunity against tumor recurrence and metastasis. All of the above results signified that Ce6-based PDT and DMC-mediated immunomodulation with ICB therapy truly increased tumor-infiltrating CTLs and decreased Tregs TME-resident to trigger a robust adaptive immune response, thus efficiently inhibiting tumor growth and *in situ* lung metastasis.

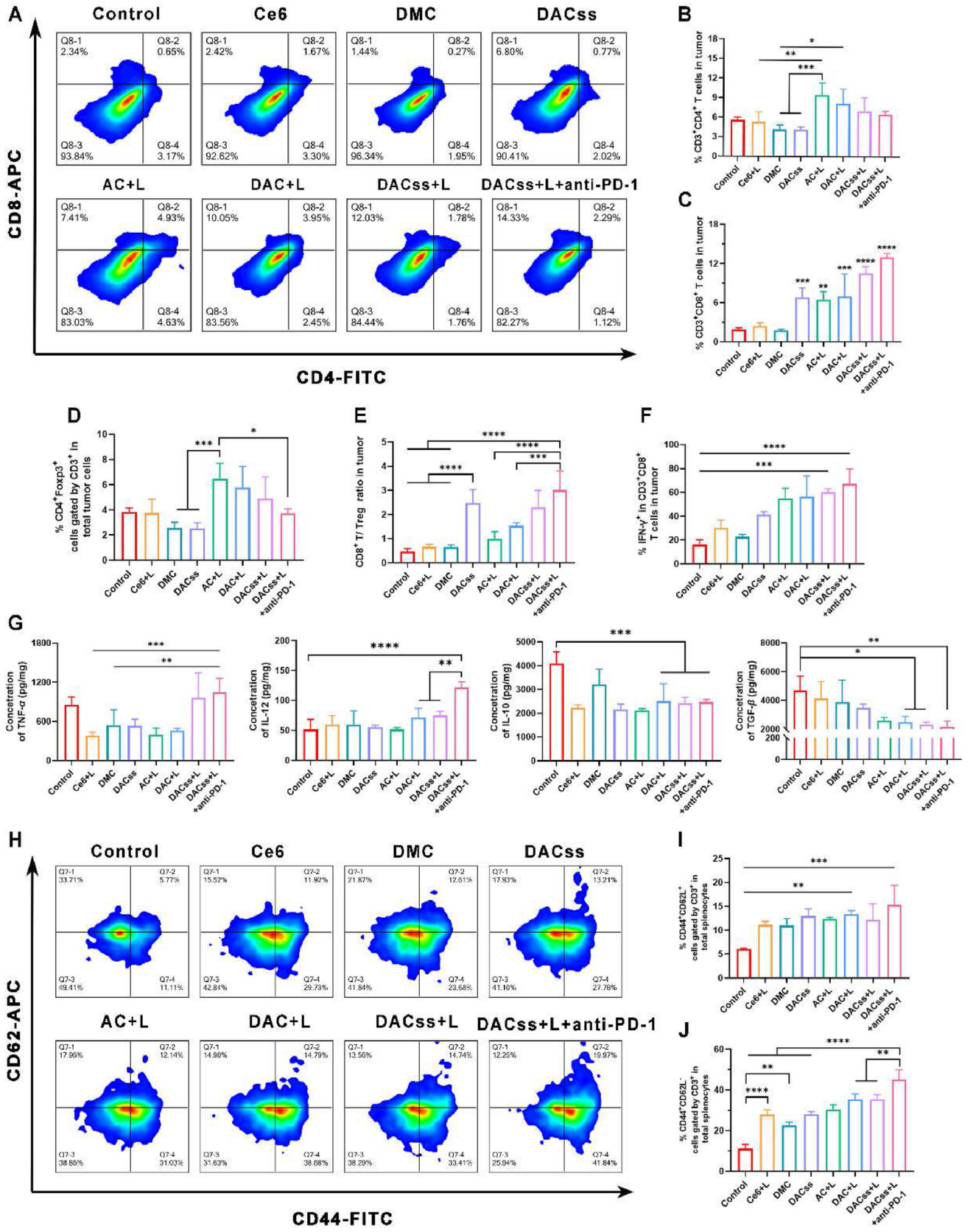

Figure 8 (A) Representative flow cytometry plots and quantification data of (B) $CD3^+CD4^+$ T cells and (C) $CD3^+CD8^+$ T cells from 4T1 tumor-bearing mice after all treatments. (D) Tregs ($CD3^+CD4^+Foxp3^+$), and (E) ratio of $CD8^+$ T to Tregs in the tumor. Percentages of (F) IFN-γ^+ after gating on $CD3^+CD8^+$ T cells. Data are shown as mean ± SD ($n = 4$). (G) Pro-inflammatory cytokines (TNF-α, IL-12) and tumor immunosuppressive cytokines (IL-10, TGF-β) levels in tumor supernatants. Data are shown as mean ± SD ($n = 3$). (H) Representative flow cytometry plots and quantification data of (I) Tcm and (J) Tem cells in spleens. Data are shown as mean ± SD ($n = 4$). $^*P < 0.05$, $^{**}P < 0.01$, $^{***}P < 0.001$, $^{****}P < 0.0001$.

4. Conclusions

In conclusion, to overcome the bottleneck of the immunosuppressive TME towards PDT, we developed a multifunctional supramolecular photodynamic nanoparticle (DACss). In terms of delivery, DACss has a dual-responsive feature. On one hand, it can release DMC in response to the acidic conditions of the TME after enrichment at the tumor site. On the other hand, it can respond to the high GSH level within the cell, leading to the disintegration of nanoparticles. This responsive-driven delivery strategy enabled DACss to achieve site-specific on-demand drug release and reduced toxicity of the photosensitizer. In terms of combination therapy, PDT, immunomodulation, and ICB therapy were combined to achieve good tumor suppression. DMC compensated for the drawbacks of the immunosuppressive TME induced by PDT, by reducing the number of Tregs in the TME as well as improving the number and activity of infiltrating $CD8^+$ T cells. The combination of PD-1 antibody mitigated the side effects of the first two, which increased the surface expression of PD-L1. The three interacted and complemented each other, ultimately achieving excellent anti-tumor and anti-*in situ* lung metastasis effects.

Acknowledgments

The work was supported by the National Natural Science Foundation of China (82173762, China), the Key Research and Development Program of Science and Technology Department of Sichuan Province (2022JDJQ0050, China), and the Fundamental of Research Funds for the Central Universities.

Author contributions

Huile Gao and Yang Zhou designed the research with the assistance of Tao Gong. Siqin He, Lulu Wang, Dongxu Wu, and Fan Tong carried out the experiments and performed data analysis. Siqin He wrote the manuscript. Huan Zhao and Hanmei Li revised the manuscript. All of the authors have read and approved the final manuscript.

Conflicts of interest

The authors have no conflicts of interest to declare.

Appendix A. Supporting information

Supporting data to this article can be found online at https://doi.org/10.1016/j.apsb.2023.10.006.

References

1. Li SM, Yang FJ, Wang YD, Du TQ, Hou XH. Emerging nanotherapeutics for facilitating photodynamic therapy. *Chem Eng J* 2023;**451**:138621.
2. Siegel RL, Miller KD, Sauer AG, Fedewa SA, Butterly LF, Anderson JC, et al. Colorectal cancer statistics, 2020. *CA A Cancer J Clin* 2020;**70**:145−64.
3. Gunaydin G, Gedik ME, Ayan S. Photodynamic therapy for the treatment and diagnosis of cancer-A review of the current clinical status. *Front Chem* 2021;**9**:686303.
4. Jia WF, Liu R, Wang YS, Hu CA, Yu WQ, Zhou Y, et al. Dual-responsive nanoparticles with transformable shape and reversible charge for amplified chemo-photodynamic therapy of breast cancer. *Acta Pharm Sin B* 2022;**12**:3354−66.
5. Yang YJ, Zhang YF, Wang R, Rong X, Liu T, Xia X, et al. A glutathione activatable pro-drug-photosensitizer for combined chemotherapy and photodynamic therapy. *Chin Chem Lett* 2022;**33**:4583−6.
6. Chen ZK, Liu LL, Liang RJ, Luo ZY, He HM, Wu ZH, et al. Bioinspired hybrid protein oxygen nanocarrier amplified photodynamic therapy for eliciting anti-tumor immunity and abscopal effect. *ACS Nano* 2018;**12**:8633−45.
7. Shi CR, Zhang QY, Yao YY, Zeng FT, Du C, Nijiati S, et al. Targeting the activity of T cells by membrane surface redox regulation for cancer theranostics. *Nat Nanotechnol* 2023;**18**:86.
8. Galluzzi L, Buque A, Kepp O, Zitvogel L, Kroemer G. Immunogenic cell death in cancer and infectious disease. *Nat Rev Immunol* 2017;**17**:97−111.
9. Ibbotson SH. Photodynamic therapy and immunosuppression. *Br J Dermatol* 2012;**167**:465−7.
10. Han LF, Huang XX, Zhu HT, Wang RY, Zhao B, Liu SX, et al. Programmed cyclodextrin-based core-shell nanoparticles for cooperative TGF-β blockade to reverse immunosuppression post photodynamic therapy. *Chem Eng J* 2023;**455**:140830.
11. Wachowska M, Muchowicz A, Demkow U. Immunological aspects of antitumor photodynamic therapy outcome. *Cent Eur J Immunol* 2015;**40**:481−5.
12. Anzengruber F, Avci P, de Freitasa LF, Hamblin MR. T-cell mediated anti-tumor immunity after photodynamic therapy: why does it not always work and how can we improve it?. *Photochem Photobiol Sci* 2015;**14**:1492−509.
13. Zhao LP, Zheng RR, Huang JQ, Chen XY, Deng FA, Liu YB, et al. Self-delivery photo-immune stimulators for photodynamic sensitized tumor immunotherapy. *ACS Nano* 2020;**14**:17100−13.
14. Peng SJ, Xiao FF, Chen MW, Gao HL. Tumor-microenvironment-responsive nanomedicine for enhanced cancer immunotherapy. *Adv Sci* 2022;**9**:2103836.
15. Xu YY, Xiong JY, Sun XY, Gao HL. Targeted nanomedicines remodeling immunosuppressive tumor microenvironment for enhanced cancer immunotherapy. *Acta Pharm Sin B* 2022;**12**:4327−47.
16. Gelderman KA, Hultqvist M, Holmberg J, Olofsson P, Holmdahl R. T cell surface redox levels determine T cell reactivity and arthritis susceptibility. *Proc Natl Acad Sci USA* 2006;**103**:12831−6.
17. Muri J, Kopf M. Redox regulation of immunometabolism. *Nat Rev Immunol* 2021;**21**:363−81.
18. von Boehmer H, Daniel C. Therapeutic opportunities for manipulating T-Reg cells in autoimmunity and cancer. *Nat Rev Drug Discov* 2013;**12**:51−63.
19. Kim HR, Park HJ, Son J, Lee JG, Chung KY, Cho NH, et al. Tumor microenvironment dictates regulatory T cell phenotype: upregulated immune checkpoints reinforce suppressive function. *J Immunother Cancer* 2019;**7**:339.
20. Almeida L, Lochner M, Berod L, Sparwasser T. Metabolic pathways in T cell activation and lineage differentiation. *Semin Immunol* 2016;**28**:514−24.
21. Raffin C, Vo LT, Bluestone JA. T-reg cell-based therapies: challenges and perspectives. *Nat Rev Immunol* 2020;**20**:158−72.
22. He SS, Li JC, Cheng PH, Zeng ZL, Zhang C, Duan HW, et al. Charge-reversal polymer nano-modulators for photodynamic immunotherapy of cancer. *Angew Chem Int Ed Engl* 2021;**60**:19355−63.
23. Cong YW, Xiao HH, Xiong HJ, Wang ZG, Ding JX, Li C, et al. Dual drug backboned shattering polymeric theranostic nanomedicine for synergistic eradication of patient-derived lung cancer. *Adv Mater* 2018;**30**:1706220.
24. Mo LJ, Zhang XJ, Shi XJ, Wei LL, Zheng DP, Li HW, et al. Norcantharidin enhances antitumor immunity of GM-CSF prostate cancer cells vaccine by inducing apoptosis of regulatory Tcells. *Cancer Sci* 2018;**109**:2109−18.

25. Fu SW, Li GT, Zang WL, Zhou XY, Shi KX, Zhai YL. Pure drug nano-assemblies: a facile carrier-free nanoplatform for efficient cancer therapy. *Acta Pharm Sin B* 2022;**12**:92−106.
26. Fu L, Ma XB, Liu YT, Xu ZG, Sun ZJ. Applying nanotechnology to boost cancer immunotherapy by promoting immunogenic cell death. *Chin Chem Lett* 2022;**33**:1718−28.
27. Zhou Y, Tong F, Gu WL, He SQ, Yang XT, Li JM, et al. Co-delivery of photosensitizer and diclofenac through sequentially responsive bilirubin nanocarriers for combating hypoxic tumors. *Acta Pharm Sin B* 2022;**12**:1416−31.
28. Yang FJ, Ji QY, Liao R, Li SM, Wang YQ, Zhang XB, et al. Precisely engineering a dual-drug cooperative nanoassembly for proteasome inhibition-potentiated photodynamic therapy. *Chin Chem Lett* 2022; **33**:1927−32.
29. Zhou Y, Zhang YW, Jiang CQ, Chen YX, Tong F, Yang XT, et al. Rosmarinic acid-crosslinked supramolecular nanoassembly with self-regulated photodynamic and anti-metastasis properties for synergistic photoimmunotherapy. *Small* 2023;**19**:2300594.
30. Liu R, Luo C, Pang ZQ, Zhang JM, Ruan SB, Wu MY, et al. Advances of nanoparticles as drug delivery systems for disease diagnosis and treatment. *Chin Chem Lett* 2023;**34**:107518.
31. Gao C, Kwong CHT, Wang QF, Kam H, Xie BB, Lee SMY, et al. Conjugation of macrophage-mimetic microalgae and liposome for antitumor sonodynamic immunotherapy *via* hypoxia alleviation and autophagy inhibition. *ACS Nano* 2023;**17**:4034−49.
32. Ding YF, Xu X, Li JY, Wang ZY, Luo JW, Mok GSP, et al. Hyaluronic acid-based supramolecular nanomedicine with optimized ratio of oxaliplatin/chlorin e6 for combined chemotherapy and O2-economized photodynamic therapy. *Acta Biomater* 2023;**164**:397−406.
33. Chen J, Li SK, Wang ZY, Pan YT, Wei JW, Lu SY, et al. Synthesis of an AIEgen functionalized cucurbit[7]uril for subcellular bioimaging and synergistic photodynamic therapy and supramolecular chemotherapy. *Chem Sci* 2021;**12**:7727−34.
34. Roy I, Bobbala S, Young RM, Beldjoudi Y, Nguyen MT, Cetin MM, et al. A supramolecular approach for modulated photoprotection, lysosomal delivery, and photodynamic activity of a photosensitizer. *J Am Chem Soc* 2019;**141**:12296−304.
35. Hu C, Cun XL, Ruan SB, Liu R, Xiao W, Yang XT, et al. Enzyme-triggered size shrink and laser-enhanced NO release nanoparticles for deep tumor penetration and combination therapy. *Biomaterials* 2018; **168**:64−75.
36. Davoodi P, Lee LY, Xu QX, Sunil V, Sun YJ, Soh S, et al. Drug delivery systems for programmed and on-demand release. *Adv Drug Deliv Rev* 2018;**132**:104−38.
37. Lu Y, Aimetti AA, Langer R, Gu Z. Bioresponsive materials. *Nat Rev Mater* 2017;**2**:16075.
38. Jiang YY, Huang JG, Xu C, Pu KY. Activatable polymer nanoagonist for second near-infrared photothermal immunotherapy of cancer. *Nat Commun* 2021;**12**:742.
39. Gao C, Wang QF, Li JY, Kwong CHT, Wei JW, Xie BB, et al. *In vivo* hitchhiking of immune cells by intracellular self-assembly of bacteria-mimetic nanomedicine for targeted therapy of melanoma. *Sci Adv* 2022;**8**:eabn1805.
40. Yuan ZT, Fan GH, Wu HL, Liu CL, Zhan YP, Qiu YY, et al. Photodynamic therapy synergizes with PD-L1 checkpoint blockade for immunotherapy of CRC by multifunctional nanoparticles. *Mol Ther* 2021;**29**:2931−48.
41. Abiko K, Matsumura N, Hamanishi J, Horikawa N, Murakami R, Yamaguchi K, et al. IFN-gamma from lymphocytes induces PD-L1 expression and promotes progression of ovarian cancer. *Br J Cancer* 2015;**112**:1501−9.
42. Ayers M, Lunceford J, Nebozhyn M, Murphy E, Loboda A, Kaufman DR, et al. IFN-gamma-related mRNA profile predicts clinical response to PD-1 blockade. *J Clin Invest* 2017;**127**:2930−40.
43. Permata TBM, Hagiwara Y, Sato H, Yasuhara T, Oike T, Gondhowiardjo S, et al. Base excision repair regulates PD-L1 expression in cancer cells. *Oncogene* 2019;**38**:4452−66.
44. Tian H, Gui YN, Wei YH, Shang B, Sun J, Ma S, et al. Z-guggulsterone induces PD-L1 upregulation partly mediated by FXR, Akt and Erk1/2 signaling pathways in non-small cell lung cancer. *Int Immunopharm* 2021;**93**:107395.
45. Zhou DF, Xiao HH, Meng FB, Li XY, Li YX, Jing XB, et al. A polymer-(tandem drugs) conjugate for enhanced cancer treatment. *Adv Healthcare Mater* 2013;**2**:822−7.
46. Qin Y, Tong F, Zhang W, Zhou Y, He SQ, Xie R, et al. Self-delivered supramolecular nanomedicine with transformable shape for ferrocene-amplified photodynamic therapy of breast cancer and bone metastases. *Adv Funct Mater* 2021;**31**:2104645.